

---

# Application of Discrete Element Method to Geomechanics

M. Jiang<sup>\*,†</sup>, H.-S. Yu<sup>\*</sup>

<sup>\*</sup> Department of Geotechnical Engineering Tongji University, Shanghai, China  
mingjing.jiang@nottingham.ac.uk

<sup>†</sup> School of Mathematics, University of Manchester, UK

**Abstract.** This chapter introduces recent application of the Distinct Element Method (DEM) to geomechanics. Different contact laws were introduced and used to investigate the noncoaxiality of granular materials, effective stress in unsaturated soils, bonding effect in natural soils and penetration mechanism in granular ground. The study shows that DEM is a promising tool to solve some difficult problems not only in fundamental geomechanics but also in complex boundary value problems in geotechnical engineering.

## 1 Introduction

Soils consist of particles, macropores, micropores, pore fluids (air, water, others), assembled possibly with interparticle bonding to form a fabric. Although soils are in essence a kind of discrete materials, they have been traditionally treated as continuum material in theoretical, constitutive modelling and numerical analyses within continuum mechanics. This method plays important role and is widely used in geotechnical engineering. However, the behaviour of soils is so complex that, although some general features are agreed upon, no particular model or theory has received universal acceptance yet.

Two types of ways have been used to consider the discrete feature of soils. The first method is to revise the available continuum models or theories by introducing additional laws which reflects the change of microstructure of soils, such as fabric [32], or by improving existing constitutive laws based on the available micromechanical studies on soils [29]. The method is usually employed by continuum constitutive modellers. In contrast, the second method treats soils as an assembly of discrete materials directly, while its macroscopic-microscopic responses under loading are obtained analytically, numerically or experimentally. This method is widely used by micromechanical researchers [5, 6, 10, 28].

In this latter method, the Distinct Element Method (DEM) becomes more and more popular, which is a numerical simulation technique originally

developed for dry granular materials by Cundall and Strack [10]. The main feature of DEM is that complex responses of an assembly of discrete materials can be controlled by very simple contact laws at interparticle contacts. For example, the Mohr–Coulomb criterion is used to control shear behaviour at contacts for dry granular materials. DEM has been used for examining several aspects of soil behaviour. Table 1 provides some application of DEM to fundamental geomechanics. Table 1 shows that DEM has been used in granular mechanics [30], creep theory [35], anisotropy of clay [33], particle crushing [7, 26], strain localization [1, 14] and dynamic behaviour or liquefaction of sands [25, 27]. To illustrate if these topics are still interesting to modern georesearchers, Table 2 presents main topics in this workshop (Modern Trends in Geomechanics workshop, 26–29 June 2005, Vienna, Austria). Table 2 shows that these topics are all discussed in this workshop. In addition, many researchers in this workshop discuss four other aspects in geomechanics: constitutive modelling, unsaturated soils, natural soils and boundary value problems. All the topics reflect the trends in geomechanics in the 21st century.

**Table 1.** Some application of DEM to fundamental geomechanics

topics	features of the study	investigators
granular mechanics	examining failure criteria of granular material; standard contact laws for granular material	Thornton (2000) [30]
creep theory	examining the theory of rate processes; contact laws incorporating creep theory	Kuhn and Mitchell [35]
anisotropy of clay	examining the mechanism of anisotropic behaviour of clay; contact laws incorporating repulsive force	Anandarajah (2000) [33]
particle crushing	examining the mechanism of particle fracture and crushing; contact laws for cementation incorporated in <i>PFC3D</i>	McDowell and Harireche (2002); Cheng et al. (2003) [7, 26]
strain localization	examining the mechanism of shear banding process; standard contact laws or that incorporating rolling resistance for granular material	Bardet and Proubet (1991); Iwashita and Oda (1998, 2000) [1, 14]
dynamic behaviour or liquefaction	regularly-packed disk assemblies considering motion of pore water or randomly-packed disk assemblies using the “quasi-pore pressure” method	Kiyama et al. (1994); Ng and Dobry (1994) [25, 27]

**Table 2.** Main topics in this workshop (Modern Trends in Geomechanics workshop, 26–29 June 2005, Vienna, Austria)

topics	presenters
granular mechanics	Bolton M, Borja R, Doanh T, Harris D, Hill J, Huang A-B, Jiang MJ, Lade P, McDowell G, Ooi J, Spencer T, Tagmanini C, Viggiani C, Wu W, Yu H-S
creep theory	Gudehus G, Yin J-H.
anisotropy	Bolton M, Doanh T, Shao J-F, Wu W
particle crushing	Bolton M, McDowell G, Vardoulakis I
strain localization	Bauer E, Bolton M, Borja R, Chambon R, Darve F
dynamic behaviour or liquefaction	Bauer E, Bolton M, Huang A-B, Niemunis A, Zhang J-M
constitutive modelling	Bolton M, Collins I, Darve F, Gens A, Gudehus G, Harris D, Herle I, Houlsby, Jiang MJ, Lade P, Niemunis A, Nova R, Puzrin AM, Selvadurai APS, Shao JF, Shen ZJ, Tagmanini C, Viggiani C, Wu W, Yin J-H, Yu H-S
unsaturated soils	Gens A, Jiang MJ, Molenkamp F, Shen ZJ, Yu H-S
natural soils	Bolton M, Huang A-B, Jiang MJ, Nova R, Shen ZJ, Yu H-S
boundary value problem	Bolton M, Harris D, Jiang MJ, Moore I, Ponter A, Salgado R, Shen ZJ, Spencer T, Yu H-S, Zhang J-M
others	Bolton M, Cristescu ND, Dafalias Y, Jiang MJ, Ooi J, Ponter A, Selvadurai APS, Shao JF, Sheng Y, Sikora Z, Triantafyllidis T, Vermeer P

The main objective of this chapter is to introduce the application of DEM to these latter four aspects in geomechanics. The introduction is limited to those related to the first author's two postdoctoral fellowships in Canada and UK. After introducing the DEM code developed by the first author, we shall present its application to noncoaxiality of granular materials, effective stress in unsaturated soils, bonding effect in natural soils and penetration mechanism in granular ground. We shall mainly introduce the target, contact models and main results in each application. The reader is referred to the references for their further detail.

## 2 Discrete Element Method (DEM)

The two-dimensional (2-D) DEM code used has techniques similar to those proposed by Cundall and Strack [10]. The code was first developed in Canada [19–21] and improved further in UK [16–18, 23, 24] by the first author and his co-workers, namely *NS2D* hereafter. Each particle of the soil mass is a rigid disk that is identified independently with its own mass,  $m$ , moment of inertia,  $I_0$  and contact properties as illustrated in Figs. 1, 4 and 8 later. The total

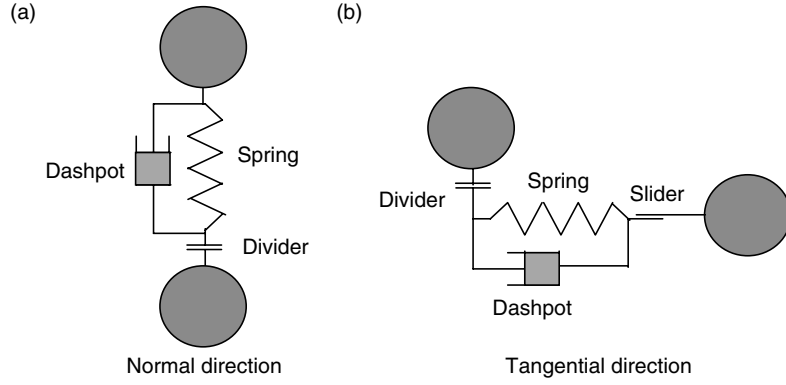


**Fig. 1.** Standard contact models of two rigid disks used in DEM for examining noncoaxial continuum model

unbalanced force for motion  $F_i^{(m)}$  ( $i$  represents  $x$  or  $y$  direction) and moment  $M_0$  acting on each particle are computed and then used to estimate the instantaneous acceleration of each particle,  $a$ , based on Newton's second law. The acceleration  $a$  is used to calculate velocities and then displacements in the  $x$  and  $y$  directions. This is repeated at each time increment until the simulation is stopped. For each particle, the normal and tangential contact forces for motion, denoted by  $F_n^{(m)}$  and  $F_s^{(m)}$ , respectively, are summed up over the  $p$  neighbours, giving:

$$\frac{\partial^2 x_i}{\partial t^2} = \frac{1}{m} \sum_{r=1}^p F_i^{(m)r}; \quad \frac{\partial^2 \theta}{\partial t^2} = \frac{1}{I_0} \sum_{r=1}^p M_0^r. \quad (1)$$

In the *NS2D* code,  $F_n^{(m)}$  is calculated by a function  $f_n$

$$F_n^{(m)} = f_n(F_n, D_n, R_n), \quad (2)$$

where  $F_n$  is the normal contact force calculated from the overlaps of particles.  $D_n$  is the normal damping force and  $R_n$  is the normal bonding strength that results from capillary water (CW) for unsaturated soil or from cementitious material for natural soils. Note that  $R_n$  is always zero for dry granular material. A typical function in (2) for unsaturated or natural soils can be expressed as

$$F_n^{(m)} = F_n + D_n - R_n, \quad (3)$$

which is termed as “translational-axis method” for bonded material [20,24].

$F_s^{(m)}$  is determined by

$$F_s^{(m)} = F_s + D_s, \quad (4)$$

where  $F_s$  is the tangential contact force and  $D_s$  is the tangential damping force.  $D_s = 0$  stands in the case that  $F_s$  exceeds the peak shear strength  $F_s^{\text{peak}}$

for contacts with intact bonds or residual shear strength  $F_s^{\text{resid}}$  for contacts without intact bonds.

$F_s^{\text{peak}}$  ( $F_s^{\text{resid}}$ ) can be described by a function  $f_s^p$  ( $f_s^r$ )

$$F_s^{\text{peak}} = f_s^p(F_n, \tan \varphi_\mu, R_t); F_s^{\text{resid}} = f_s^r(F_n, \tan \varphi_\mu), \quad (5a,b)$$

where  $\tan \varphi_\mu$  is called the interparticle friction coefficient.  $R_t$  is the tangential bonding strength that results from CW for unsaturated soil or from cementation material for natural soils. Typical functions in (5) for dry granular material and natural soils can be respectively expressed as

$$F_s^{\text{peak}} = F_n \tan \varphi_\mu = F_s^{\text{resid}} \quad \text{for dry granular material,} \quad (6a,b)$$

$$F_s^{\text{peak}} = F_n \tan \varphi_\mu + R_t; F_s^{\text{resid}} = F_n \tan \varphi_\mu \quad \text{for natural soils} \quad (6c,d)$$

Equation (6) are the Mohr–Coulomb criterion. If two particles are separated due to normal tension force in excess of  $R_n$ , then  $F_n^{(m)} = 0$ ,  $F_s^{(m)} = 0$ . Damping, as well as frictional sliding, is used in DEM analyses to dissipate energy due to the dynamic formulation of the model.

The strain tensor is obtained by the position change of rigid boundaries as follows:

$$\varepsilon_{ij} = \Delta h_i / h_j, \quad (7)$$

where  $\Delta h_i$  is the deformation of specimen in  $i$  direction and  $h_j$  is total length of specimen in  $j$  direction at time  $t$ .

The stress tensor is defined on the rigid boundaries as follows:

$$\sigma_{ij} = (\sum f_i) / h_j, \quad (8)$$

where  $f_i$  is the contact force acting on the boundary with the normal direction as  $i$ . In addition, a unit of length (m) is implicitly included in (8) in the direction vertical to the plane.

Because *NS2D* is a 2-D DEM code, the density of specimen is described in term of planar void ratio  $e_p$  by

$$e_p = (A - A_g) / A_g, \quad (9)$$

where  $A$  and  $A_g$  are the total area of the specimen and the sum of the area of all grains (disks), respectively.

*NS2D* can form an assembly of particles according to its grain size distribution. The number of particles of each specific radius was calculated in the DEM by

$$N_{(i)} = \frac{P_{(i)}}{r_{(i)}^s \cdot P} \cdot N, \quad (10)$$

where  $N_{(i)}$  is the total number of particle  $i$  with specific radius  $r_{(i)}$  and  $P_{(i)}$  is weight percentage of particle  $i$ .  $N$  is total number of particles of different

radii used in the DEM analyses. Parameter  $s$  is 2 for disk.  $P$  is a variable obtained by

$$P = \sum_{i=1}^{n_p} \frac{P_{(i)}}{r_{(i)}^s}, \quad (11)$$

where  $n_p$  is the type number for particles.

We shall in Sect. 3 introduce the application of *NS2D* to geomechanics, which are related to the four topics in this workshop.

### 3 Application of DEM to Geomechanics

In this section, we shall present the application of DEM to noncoaxiality of granular materials, effective stress in unsaturated soils, bonding effect in natural soils and penetration mechanism in granular ground. We shall introduce each application by its target, contact model and main results

#### 3.1 Noncoaxiality of Granular Materials

Noncoaxiality means the noncoincidence of the principal stress tensor and the principal plastic deformation-rate tensor, a known feature of granular material. Since granular materials are inherently *discrete* with *particle rotation* and a grain length scale, we shall examine if these features can be included in a noncoaxial continuum model. The detailed information can be found in the references [17, 18].

Given a randomly packed assembly composed of particles of different sizes, a novel kinematic variable, the “*averaged micropure rotation-rate*” (APR), denoted by  $\omega_3^c$ , was proposed as follows [17]

$$\omega_3^c = \frac{1}{N} \sum_{k=1}^N \dot{\theta}^k = \frac{1}{N} \sum_{k=1}^N \left[ \frac{1}{r^k} \left( \dot{\theta}_1^k r_1^k + \dot{\theta}_2^k r_2^k \right) \right], \quad (12)$$

where the summations are over the  $N$  contacts in the mass body, by counting each contact  $k$ , which is shared by two particles of radii  $r_1^k$  and  $r_2^k$ , the angular velocity  $\dot{\theta}_1^k$  and  $\dot{\theta}_2^k$ . The common radius is  $r^k = 2r_1^k r_2^k / (r_1^k + r_2^k)$ .  $\omega_3^c$  can also be expressed in terms of a sum over particles instead of contacts [21]. It is a kinematic variable generally related to particle rotations and particle sizes, which does not appear in classical continuum mechanics yet. But, it can be unified with kinematic variables in standard continuum mechanics, see later.

In standard continuum mechanics, the Eulerian velocity field  $v$  is considered. The deformation rate  $D_{ij}$  and the spin tensor  $W_{ij}$  are then defined by

$$D_{ij} = \frac{1}{2} \left( \frac{\partial v_i}{\partial x_j} + \frac{\partial v_j}{\partial x_i} \right); \quad W_{ij} = \frac{1}{2} \left( \frac{\partial v_i}{\partial x_j} - \frac{\partial v_j}{\partial x_i} \right), \quad (13a,b)$$

where  $v_i$  denotes the velocity components, with  $i$  or  $j = 1, 2$  in the 2-D case.

We propose a tensor  $R_{ij}$  as follows:

$$R_{ij} = \frac{\partial v_i}{\partial x_j} + e_{3ij}\omega_3^c, \quad \text{where} \quad e_{3ij} = \begin{bmatrix} 0 & 1 \\ -1 & 0 \end{bmatrix}, \quad (14a,b)$$

which leads to the symmetric (skew-symmetric) tensor  $d_{ij}$  ( $w_{ij}$ ) by

$$d_{ij} = \frac{1}{2}(R_{ij} + R_{ji}); \quad w_{ij} = \frac{1}{2}(R_{ij} - R_{ji}) \quad (15a,b)$$

Relationships amongst  $D_{ij}$ ,  $W_{ij}$ ,  $d_{ij}$  and  $w_{ij}$  can be obtained from (13)–(15)

$$d_{ij} = D_{ij}; \quad w_{ij} = W_{ij} + e_{3ij}\omega_3^c \quad (16a,b)$$

which shows that  $d_{ij}$  indeed is deformation rate tensor.  $w_{ij}$  is a frame indifferent tensor composed of both  $W_{ij}$  and  $\omega_3^c$ , even though none of them is an objective continuum variable. When  $\omega_3^c = 0$ , the tensor  $w_{ij}$  will reduce to  $W_{ij}$ .

We shall present a new noncoaxial continuum model for granular material [17], which is based the unified double-slip plasticity model [36] and the  $d_{ij}$  and  $w_{ij}$ . The unified kinematic equations governing the velocity field proposed by Harris (1995) are

$$(D_{11} + D_{22}) \cos \left( \frac{\nu + \xi}{2} \right) = [(D_{11} - D_{22}) \cos 2\psi_\sigma + 2D_{12} \sin 2\psi_\sigma] \\ \times \sin \left( \frac{\nu - \xi}{2} \right), \quad (17a)$$

$$2(\vartheta + W_{12}) \sin \left( \frac{\nu + \xi}{2} \right) = [(D_{11} - D_{22}) \sin 2\psi_\sigma - 2D_{12} \cos 2\psi_\sigma] \\ \times \cos \left( \frac{\nu - \xi}{2} \right), \quad (17b)$$

where the quantities  $\nu$  and  $\xi$  are material parameters, and  $\vartheta$  is an angular velocity which may be given a number of physical interpretations.  $D_{ij}$  and  $W_{ij}$  are the deformation rate tensor and the spin tensor respectively as shown in (13). The principal stress inclination  $\psi_\sigma$  is defined as the angle of major principal stress axis to  $x$ -axis, in terms of Cauchy stress tensor  $\sigma_{ij}$

$$\psi_\sigma = \frac{1}{2} \arctan \left( \frac{2\sigma_{12}}{\sigma_{11} - \sigma_{22}} \right). \quad (18)$$

The new continuum model was proposed in essence by identifying the quantity  $\vartheta$  in (17) with  $\omega_3^c$ . By further choosing  $\nu = \phi$ , the angle of internal friction,  $\xi = \phi - 2\chi$  where  $\chi$  is a dilatancy parameter, and (15), the new model

for a class of dilatant materials, becomes

$$(d_{11} + d_{22}) \cos(\phi - \chi) = [(d_{11} - d_{22}) \cos 2\psi_\sigma + 2d_{12} \sin 2\psi_\sigma] \sin \chi, \quad (19a)$$

$$2w_{12} \sin(\phi - \chi) = [(d_{11} - d_{22}) \sin 2\psi_\sigma - 2d_{12} \cos 2\psi_\sigma] \cos \chi, \quad (19b)$$

or further reduced for incompressible materials,

$$d_{11} + d_{22} = 0; \quad 2w_{12} \sin \phi = (d_{11} - d_{22}) \sin 2\psi_\sigma - 2d_{12} \cos 2\psi_\sigma \quad (20a,b)$$

Equations (19b) or (20b) show that, generally, the constitutive equations for granular materials presented here are noncoaxial due to the presence of  $w_{ij}$ . Since the original unified plasticity model is called the double-slip model and now is extended by  $\omega_3^c$ , the new model may be called the “*double-slip and rotation-rate model*” (DSR<sup>2</sup> model).

The NS2D was used to carry out tests to verify the DSR<sup>2</sup> model, since no geolab technology is available to measure  $\omega_3^c$  yet. The contact model used is a standard contact laws shown in Fig. 1. This simple contact model consists of a normal (tangential) contact model to resist traction (shear) force. They are similar in their principle: both include a spring reflecting an elastic behaviour of the contact before failure and a dashpot that allows energy dissipation and quasi-static deformations in DEM analyses. The normal contact model includes a divider to simulate the fact that no traction force is transmitted through the contact when the particles are separated. The tangential contact model includes a slider that provides the contact a shear resistance controlled by the Mohr–Coulomb criterion.

The granular material used has a distribution of particle size shown in Fig. 2a. The material is composed of discs with a maximum diameter of

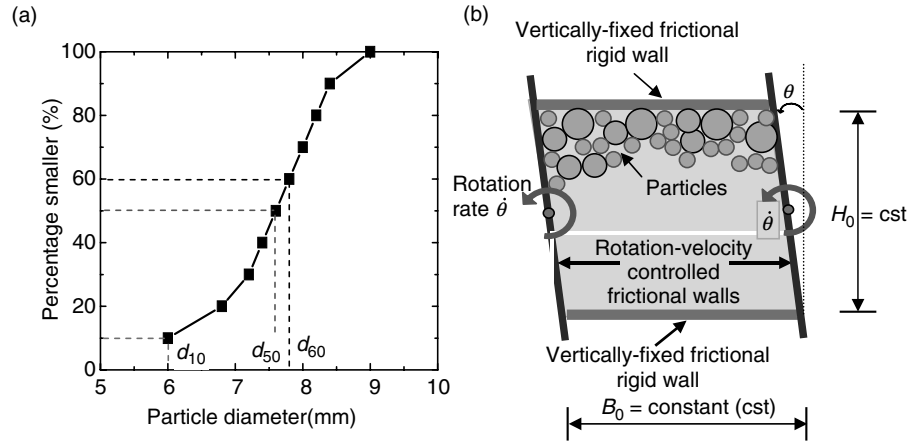


**Fig. 2.** Distribution of grain size used in DEM verification on noncoaxial models (a); boundary conditions in simple shear stage (b)

9.0 mm, and a minimum diameter of 6.0 mm, an average grain diameter  $d_{50} = 7.6$  mm and uniformity coefficient  $d_{60}/d_{10} = 1.3$ . For simplicity, simple shear tests were simulated for the verifications, in which the specimens are regarded to be “incompressible”, i.e. their volume change is zero under shear. The incompressibility is targeted by (a) selecting specimens that internally tends to perfect plasticity with its dilatancy–contractancy close to zero; (b) controlling boundary condition that the volumetric strain rate is zero under shear. The samples were prepared by the under-compaction technique [19], which efficiently provided homogeneous loose/medium-dense samples ( $e_p = 0.32/0.30$ ). The boundary condition in the simple shear stage is shown in Fig. 2b. The particle-wall friction coefficient was set to a value of 0.5, the same value as the interparticle friction coefficient, followed by simple shear under constant volume. The top and bottom rigid walls were vertically fixed, but moved horizontally by following the side rigid walls which rotated with rotation rate  $\dot{\theta}$ . Monotonic and cyclic simple shear tests were carried out with different variations of  $\dot{\theta}$ . Using (13), (16), (20b) and theoretical description of velocity field under simple shear, the theoretical APR predicted by the DSR<sup>2</sup> model may be written:

$$\text{APR} = \left( \frac{\cos 2\psi_\sigma}{2 \sin \phi} + \frac{1}{2} \right) \dot{\theta}, \quad (21)$$

which, as well as  $\omega_3^c$ , can be obtained in the DEM tests [18].

Figure 3a provides the APRs measured and predicted by the DSR<sup>2</sup> model for the medium-dense specimen in the monotonic DEM tests, and their respective average values for all specimens deduced from all the monotonic DEM tests. For the predicted values,  $\phi = 30^\circ$  was used in (21), which is very close to that measured in experiments on granular materials. Figure 3a shows that although there is very slight difference between the predicted and measured APRs, a good agreement appears between these quantities during the DEM tests. Both of them are positive, and decrease slightly with the shear strain in the tests. Good agreement is also observed between the predicted and the measured APRs in the tests on all the other specimens of different density. For conciseness, the average values of the predicted and the measured APRs are provided in Fig. 3a to represent these results. Again, a good agreement is evidently observed in Fig. 3a between the predicted and the measured values.

Figure 3b presents the APRs measured and predicted by the DSR<sup>2</sup> model in the cyclic DEM simple shear tests on loose/medium-dense specimens. Figure 3b shows that there is also a good agreement between these predicted and measured quantities in the DEM tests. They are both periodic, varying between 0.0025 and  $-0.0025 \text{ rad s}^{-1}$  with the same period during cyclic shear tests on the different specimens. Hence, the numerical results in Fig. 3 confirm that: (a) DSR<sup>2</sup> model is a reasonable extension of the unified double-slip plasticity model; (b) DEM is a useful tool in examining the noncoaxiality of granular materials.

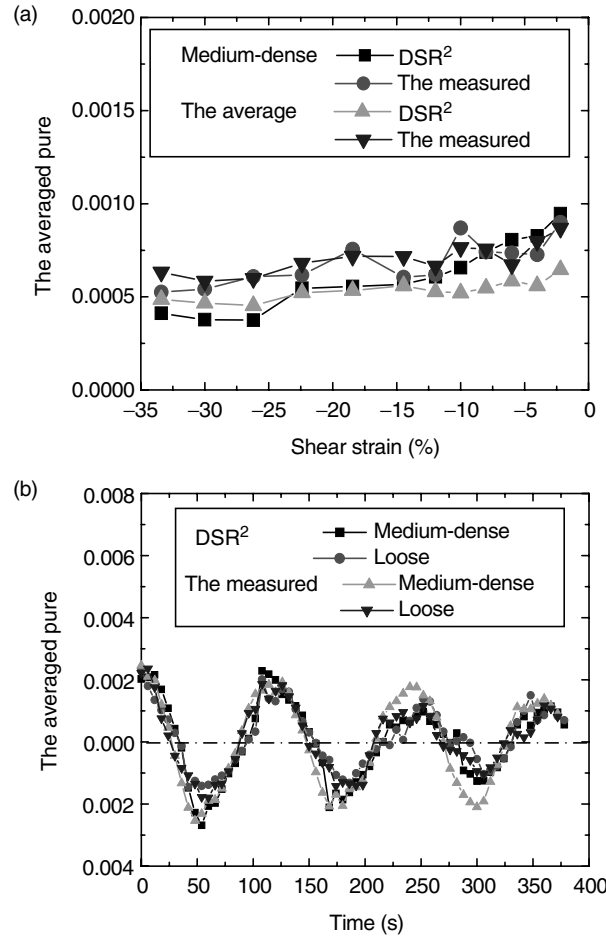


**Fig. 3.** The APRs measured and predicted by noncoaxial models (DSR<sup>2</sup> model) for the medium-dense specimen, and their respective average values for all specimens in the all monotonic DEM simple shear tests (a); the measured and the predicted APRs in the cyclic DEM simple shear tests on loose/medium-dense specimens (b)

### 3.2 Effective Stress in Unsaturated Soils

One of long-term arguable topics in unsaturated soils is the existence and applicability of effective stress [13, 15]. We shall here introduce micromechanically defined effective stress and its verification by DEM from the viewpoint of strength. In the definition, the interparticle force due to CW is composed of two components: one due to suction and the other due to the surface tension which is missing in unsaturated soil mechanics.

Equation (8) is widely used in geolabs to measure stresses. This stress tensor is equivalent to net stress ( $\sigma_{ij} - u_a$ ) used in unsaturated soil mechanics

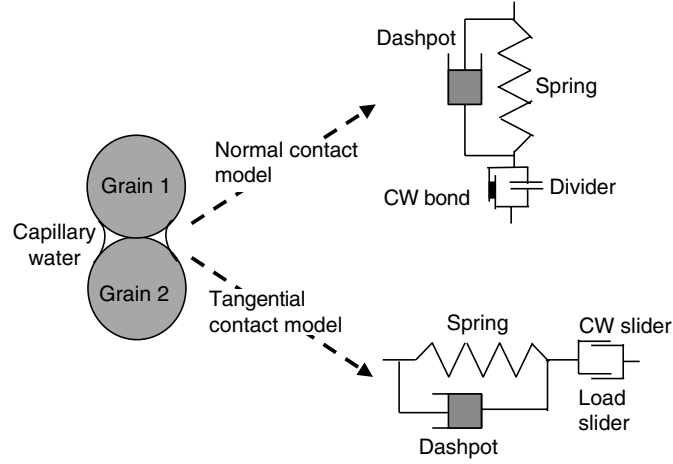


Fig. 4. Contact model for CW [20]

because the pore air pressure  $u_a$  is used as a reference pressure and is effectively zero in many practical problems. In contrast, in micromechanics on dry granular media, there are several expressions of the stress tensor, and controversies still exist on such topics as the asymmetry [2, 6, 11]. We consider three symmetric average stress tensors with all defined within the volume  $V$ :

$$\sigma_{ij} = \frac{1}{V} \sum_{k=1}^N R_k \sum_{c=1}^p l_i^c T_j^c; \quad \sigma_{ij} = \frac{1}{V} \sum_{a=1}^M T_i^a l_j^a; \quad \sigma_{ij} = \frac{1}{V} \sum_{a=1}^{2M} x_i^a T_j^a \quad (22a, b, c)$$

where  $T_i^c$  and  $l_j^c$  are the contact force vector and the contact orientation vector at contact  $c$  of particle  $k$ .  $R_k$  is the radius of particle  $k$ .  $N$  is the number of particles in  $V$  and  $p$  is the number of contacts on particle  $k$  [10].  $M$  is the number of contacts in  $V$ .  $T_i^a$  and  $l_j^a$  are the contact force vector and the contact orientation vector at contact  $a$  in  $V$  [8].  $x_i^a$  defines the coordinates of contact  $a$  referenced to the particle centroid [31].

Nevertheless, the average stress tensors in (22) are all equivalent to that by computing the forces exerted upon the peripheral particles along the assembly's boundary  $S$ .

$$\sigma_{ij} = \frac{1}{V} \sum_{\beta \in S} T_i^\beta l_j^\beta. \quad (23)$$

Based on (22)–(23) and the concepts proposed by one of the authors [22], two new stress tensors have been defined by Jiang et al [16, 21]. The first one is defined as the stress tensor in (22) or (23) when  $T_i^c$  ( $T_i^a$  or  $T_i^\beta$ ) is the interparticle force due to *both load and CW*, then  $\sigma_{ij} = \sigma_{ij}''$ . It is termed generalized effective stress (GES) and denoted by  $\sigma_{ij}''$  here to distinguish it from the effective stress  $\sigma_{ij}'$  used in saturated soil mechanics. The second one is

defined as the stress tensor in (22) or (23) when  $T_i^c$  ( $T_i^a$  or  $T_i^\beta$ ) is equal to interparticle force *solely due to CW*, then  $\sigma_{ij} = \sigma_{ij(eq)}$ . It is termed the GES due to suction (GESS) here to follow the habit in geomechanics. The *GES due to suction* indeed should be referred to as the *GES due to CW* since the interparticle force component due to the surface tension is included, based on the theoretical work by Fisher [12]. The stress  $\sigma_{ij(eq)}$ , in principle, is similar to other terms, such as “normal stress”, “equivalent effective stress”, “effective boundary stress” etc. used in the literature to describe the effect of suction on shear strength. We use a subscript “eq” in  $\sigma_{ij(eq)}$  to note that GESS is similar to “equivalent effective stress” in essence. Note that both GES and GESS are defined explicitly in terms of interparticle forces via (22) or (23) here. More importantly, interparticle force due to CW is a theoretical solution [12], composed of components due to both the suction and the surface tension. We shall next introduce DEM examination on the strength envelopes of unsaturated soils described in different stress tensors, since no geolab technology is available for this task yet.

The contact model used for unsaturated soils is illustrated in Fig. 4, which was proposed by Jiang et al. [21]. It also consists of a normal (tangential) contact model to resist traction (shear) force. Compared with the standard model in Fig. 1, the normal contact model introduces additionally a bond element to represent the action of CW whereas the tangential contact model includes a CW slider. No traction/repulsive force is transmitted when the CW bond is broken and the particles are separated. The tangential contact model includes two sliders that provide the contact a shear resistance controlled by the Mohr–Coulomb criterion, with one component linked to the CW and the other to the load. The introduction of the CW slider comes from the fact that the interparticle force due to CW increases the normal contact force at contact and thus consequently its shear resistance. Note that the CW bond is recoverable after its breakage, i.e. the CW bond recovers once particles contact again. The introduction of the CW bond and slider will lead to mechanical performance at the contact as elasto-brittle-plastic in normal and elasto-plastic in shear directions [21].

The particle assemblies of grain size distributions shown in Fig. 5 were used. They are fine-sized materials of the same mean diameter  $d_{50}$  as 0.0078 mm, but of different uniformity coefficients  $d_{60}/d_{10}$  as 1.3 for Distribution A and as 1.8 for Distribution B. A series of biaxial compression tests were carried out on the unsaturated granulates under different suctions and different confining stress. Note that, during the tests, the disappearance of manisci is simulated [21].

The peak shear strength envelopes described by net stresses (total stress over air pressure), i.e. the stresses defined in (8), are plotted in Fig. 6a, which are deduced from the biaxial compression tests on material A. Figure 6a shows that, for the material with zero suction ( $S_u$ ), the shear strength envelope almost passes through the origin, confirming that the material is cohesionless. The peak shear strength envelopes move parallel to each other with the

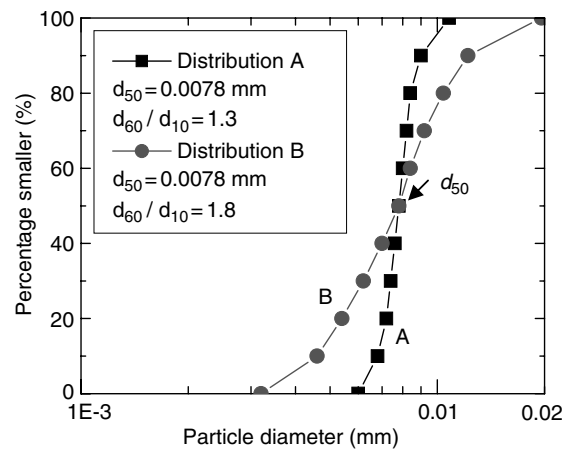


**Fig. 5.** Grain-size distributions used in the DEM analyses on unsaturated soils

increase of  $S_u$  in the direction of increasing peak shear strength. A nonlinear relationship is observed between the deduced apparent cohesion and  $S_u$  in Fig. 6b, which is in agreement with the observations from experiments.

The peak shear strength envelope described by the GES are illustrated in Fig. 7a, which are deduced from the same tests on material A as in Fig. 6. Figure 7a indicates that there appears to be a unique peak strength envelope for all the tests on the same material, even with different consolidation stress or different suction ( $S_u$ ). In addition, the peak friction angle deduced from this envelope is equal to  $27.4^\circ$ , very close to that deduced from the zero-suction envelope ( $26.5^\circ$ ) for the same material shown in Fig. 7a. In addition, Fig. 7b provides the peak strength envelope described by GES, deduced from 12 tests on material B. Figure 7b demonstrates that the results obtained from material B support the observations made for material A. Furthermore, Fig. 7 shows that there is also a unique residual shear strength envelope for each material if it is described in terms of GES. These observations seem to support the existence of “effective stress” for unsaturated soils [3] in controlling the shear strength. However, it is easy to realize that there is a difference between the original definition [3] and the definition given via (22) or (23). Since the applicability of the principle of effective stress has been debated for a long time [13, 15], it is beyond the purpose of this chapter to give any comments on the topic here. Hence, Figs. 6 and 7 show that DEM is a useful tool in examining the effective stress in unsaturated granular materials.

### 3.3 Bonding Effect in Natural Soils

Natural soils are sometimes named as “problematic soil”, since their mechanical behaviour are evidently distinct from the reconstituted soils usually employed in laboratory. Their peculiar behaviour results from their

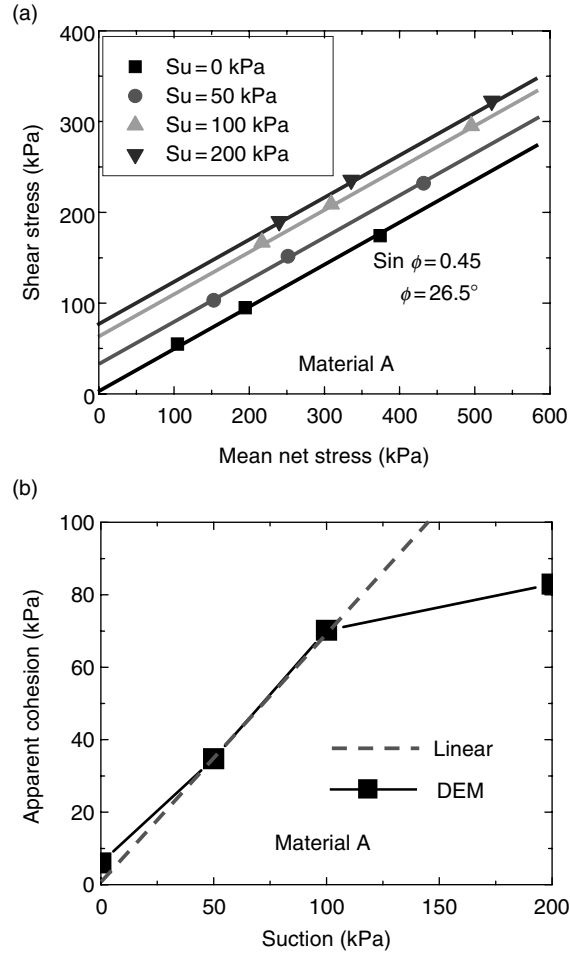


**Fig. 6.** Peak shear strength envelopes described by net stresses  $[(\sigma_v - \sigma_h)/2, (\sigma_v + \sigma_h)/2 - u_a]$  (a), and relationship between apparent cohesion and suction ( $S_u$ ) (b), obtained from biaxial compression tests on specimens of unsaturated material A

microstructure which is mainly characterized with bonding materials between particles or aggregates (bonds) and fabric. In this subsection, we shall present our most recent DEM application to natural sands: the link between the yielding and bond breakage; the Coop and Willson criteria on weak bonding and strong bonding [9]. The reader is referred to the reference [24] for further detail and other information. We chose DEM, because no geolab technology is available to measure bond information quantitatively and continuously yet.

The contact model used for bonds in natural soils is shown in Fig. 8, which was proposed by Jiang et al. [20, 24]. In comparison to the standard contact model in Fig. 1, the bond contact model introduces irrecoverable rigid-plastic

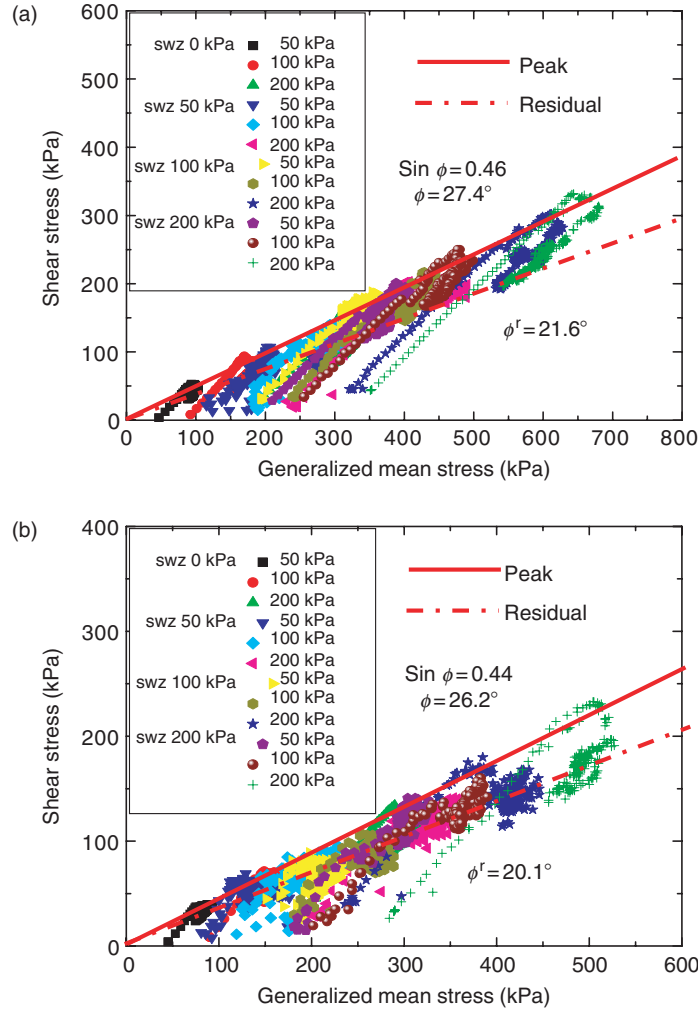


**Fig. 7.** Peak/residual shear strength envelopes under different suctions ( $S_u$ ), described by the GES  $((\sigma_v'' - \sigma_h'')/2, (\sigma_v'' + \sigma_h'')/2)$ , obtained from biaxial tests on unsaturated specimens of distribution A (a) and distribution B (b)

bond elements into the normal and tangential directions, respectively. Unlike the recoverable CW bond shown in Fig. 4, the bond here is irrecoverable, i.e. the bond will never recover its strength once the bond breaks. The rigid bond element is set to be parallel with divider (slider) in the normal (tangential) contact model to produce tension (shear) resistance, which represents the main action of bonding materials. The introduction of the bonds will lead to mechanical performance at the contact as elasto-brittle-plastic in both normal and shear directions [20, 24].

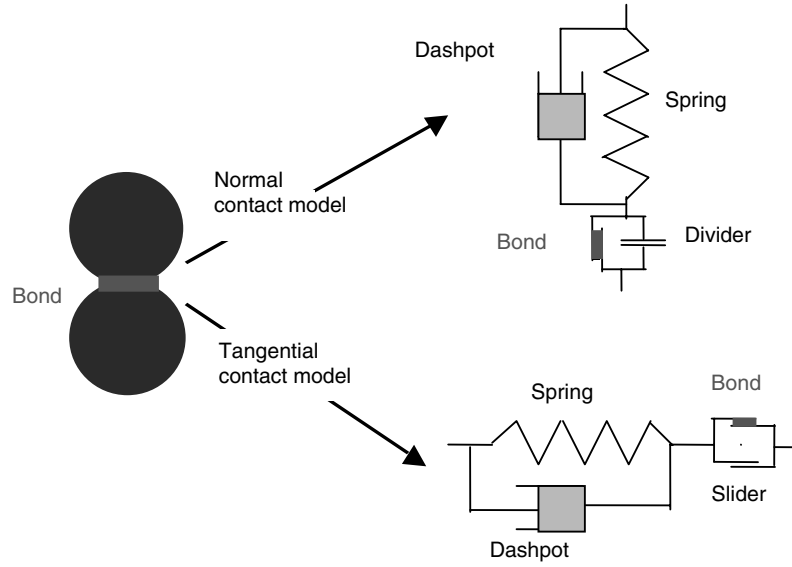


**Fig. 8.** Contact model proposed for bonds in natural soils [20]

The DEM material used has a distribution of particle size shown in Fig. 2a. The samples were prepared by the under-compaction technique [19] at very loose (planar void ratio  $e_p = 0.34$ ), loose (0.32), medium-dense (0.30) and dense (0.28) states, followed by bonding at contacts with different bonding strength. Isotropic consolidation tests were carried out on these bonded material, by following the procedure in laboratory [24].

For the first target in this subsection, Fig. 9a presents the variation of planar void ratio  $e_p$  with applied mean stress  $\sigma'_m$ , whereas Fig. 9b provides the broken contact ratio as a function of  $\sigma'_m$ , for the very-loose DEM materials of the bonding strength  $R = 0, 1, 5, 10, 20, 30$  MN. The broken contact ratio is the proportion of the initially-bonded contacts that have been broken and can be regarded as a damage index of the bond breakage. The numerical curve obtained for the very-loose unbonded material in Fig. 9a provides a reference curve (normal compression line, NCL) for the other DEM tests. This numerical reference curve shows three features: there is a significant reduction in void ratio ( $e_p$ ) against  $\sigma'_m$  when the pressure is relatively small ( $< 0.4$  MPa); once  $\sigma'_m$  exceeds this value, the rate of void ratio reduction becomes smaller; this is true until the pressure is close to 10 MPa when the void ratio reduction rate increases again. The second feature in the DEM data comes from that there is a little space for the assembly to be compacted further as it arrives at a relative dense state. The third feature of the numerical reference curve appears to be unusual. This peculiar feature is largely due to the fact that overlap between particles is excluded from calculating  $e_p$  by (9). Nevertheless, such ignorance does not affect the difference between bonded and unbonded materials.

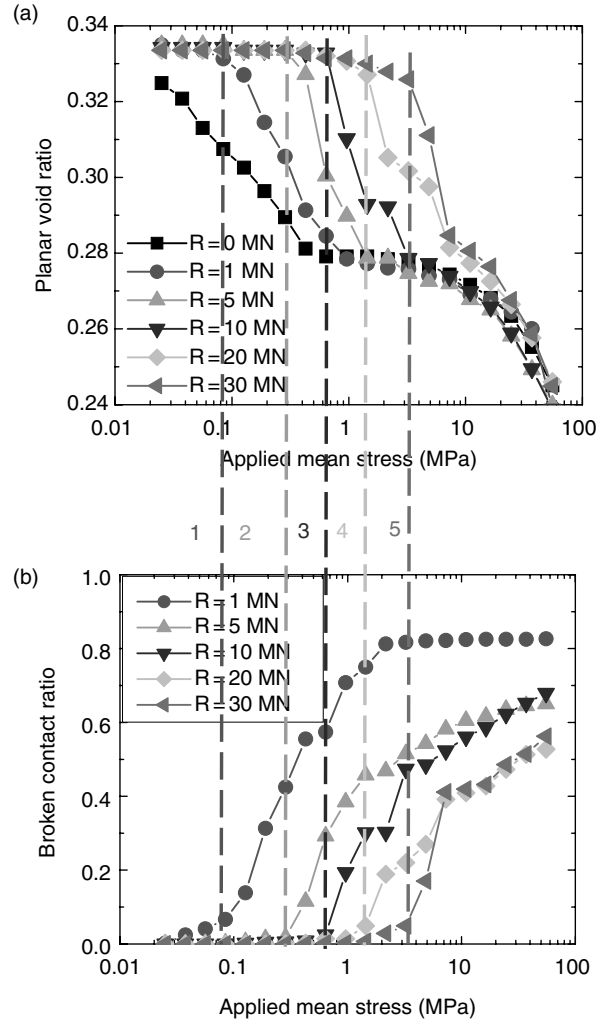


**Fig. 9.** The yielding observed in the DEM isotropic compression tests on very-loose materials of different bonding strengths from: (a) compression curves; (b) broken contact ratio

The bonded materials in Fig. 9a shows that the gross-yielding stress is well defined in light of volumetric strain (also known as *preconsolidated pressure* in the geotechnical community). They are able to go in part of the  $e_p - \sigma'_m$  space that is not accessible to the unbonded material. At a given consolidation pressure, their void ratio is generally larger than unbonded counterpart. The preyield deformation is small; deformation increases abruptly if consolidation pressure is larger than the yield stress. Given a void ratio, the gross-yielding stress increases with the bonding strength. These are in agreement with the recent understanding on natural soils.

Micromechanically, Fig. 9b shows that the yielding can also be well defined for the samples in terms of breakage of bonds (the most-gradient point on the curve) for bonded specimens, which namely the microyielding hereafter. There is no or few bond breakage when  $\sigma'_m$  is smaller than the microyielding stress. Once  $\sigma'_m$  exceeds the microyielding stress, a large amount of bonds break. By comparing Fig. 9a with Fig. 9b, with the help of the dotted lines 1–5 in Fig. 9, it is observed that the microyielding stress appears to be equal to or slightly smaller than the respective gross yielding stress. Hence, the DEM results confirm that the gross yielding of natural sands must be related to bond breakage.

For the second target in this subsection, Fig. 10 provides schematic representation of the factors that might influence the effect of inter-particle cementing on the compression behaviour of a natural sand, proposed by Coop and Willson [9]. Figure 10 shows that a yield point in compression may be above (outside) or below (inside) NCL. The former one is termed as strong bonding (s), while the latter as weak bonding (w). They believe that whether the bonding is weak or strong depends on three factors, which, if regardless of particle breakage/crushing, are:

- (a) The amount and strength of the cement deposited, with a smaller amount clearly being present for the weak bonding while a larger amount for the strong bonding, as indicated in Fig. 10a;
- (b) The position of NCL. The same yield stress may be regarded as strong bonding if NCL is inside it, or weak bonding if NCL is outside, as shown in Fig. 10b;
- (c) The initial density. A denser bonded material, even though it has the higher yield stress in compression, may show the weak mode of behaviour, whereas a looser bonded material of the lower yield stress may show the strong mode, as demonstrated in Fig. 10c.

Figure 11 presents the variation of  $e_p$  with  $\sigma'_m$  in the isotropic DEM compression tests, showing the three factors influencing the effect of bonds on the compression behaviour. Note that all materials are of the same coefficient of interparticle friction as  $\mu = 0.5$ , except specifically stated below. It can be seen:

- (a) In Fig. 11a that the DEM medium-dense material predicts a weak bonding behaviour at bonding strength  $R = 1$  MN but a strong bonding behaviour at  $R = 10$  MN. This confirms the first Coop and Willson criterion concerned with the amount and strength of the cement.
- (b) In Fig. 11b that the response of the two unbonded very loose materials shows that NCL of  $\mu = 0.5$  (NCL1 in the figure) is well above that of  $\mu = 0.2$  (NCL2 in the figure), which is reasonable since larger  $\mu$  produces larger resistance against compaction under a give pressure. The two bonded DEM medium-dense materials, which have  $R = 1$  MN for  $\mu = 0.5$  (Material 1) and  $R = 1.5$  MN for  $\mu = 0.2$  (Material 2), respectively, predict almost the same gross yielding stress, with the compression curves approaching their own NCL after yielding. In addition, the gross yielding

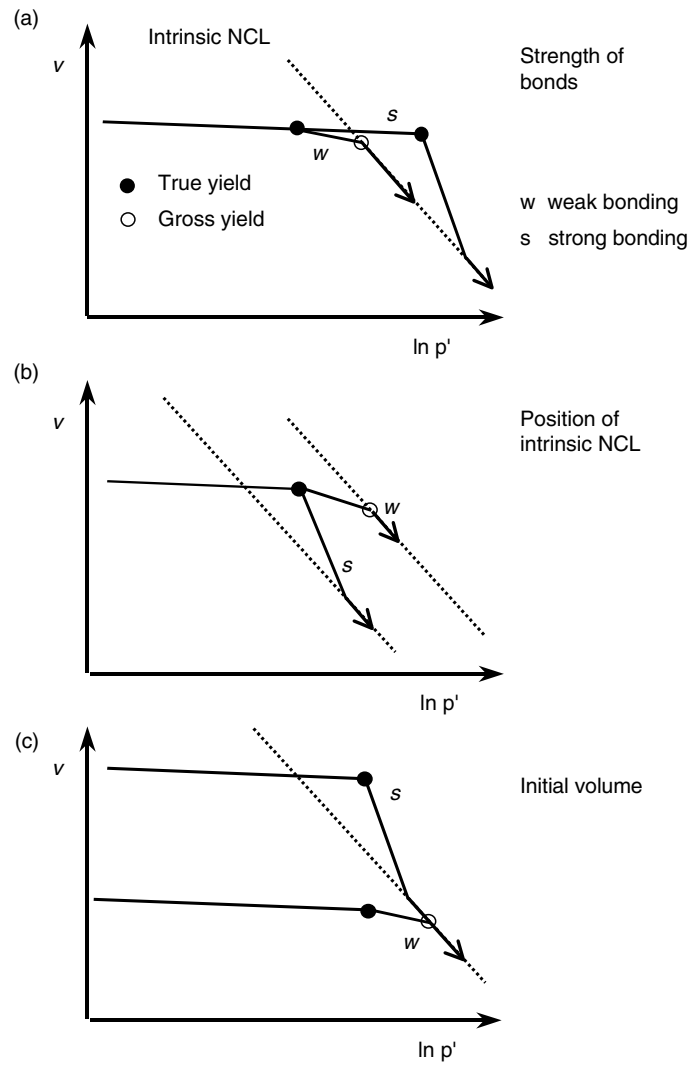


**Fig. 10.** Weak bonding (w) and strong bonding (s) criteria used by Coop and Willson [9] in investigating the factors might influence the effect of bonds on the compression behaviour of a sand: strength of bonds (a); position of NCL (b); initial volume (c). (after Coop and Willson [9])

stress of the two bonded materials lies between NCL1 and NCL2, indicating that Material 1 should be regarded as a weak bonding since NCL1 is outside it, while Material 2 a strong bonding since NCL2 is inside it. This confirms the second Coop and Willson criterion concerned with the position of the intrinsic NCL.

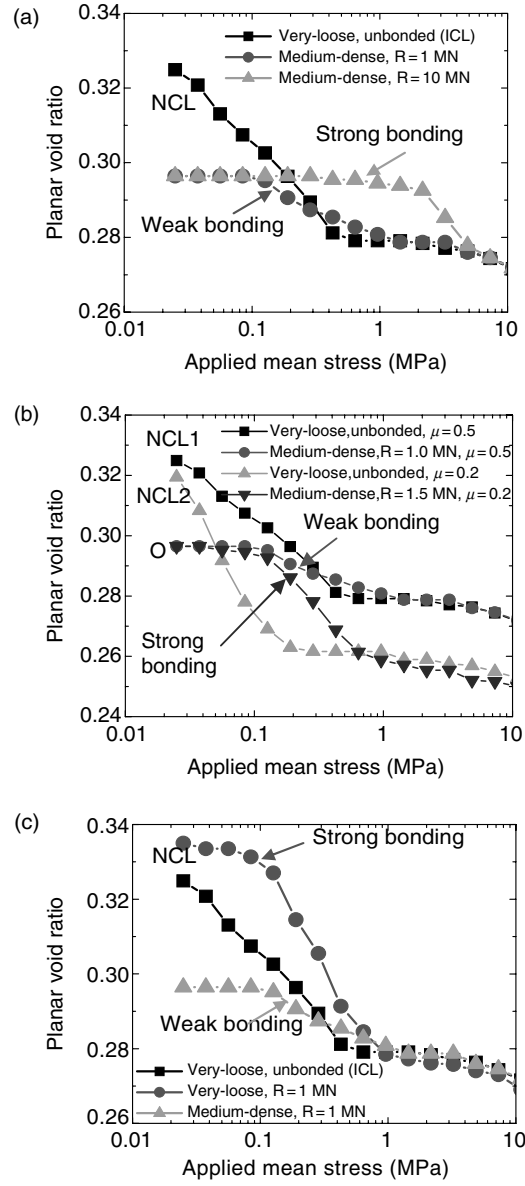


**Fig. 11.** The factors influencing the effect of bonds on the compression behaviour observed in the DEM tests on bonded materials: strength of bonds (a); position of NCL (b); and initial density (c)

- (c) In Fig. 11c that the very-loose bonded DEM material, even though it has the lower yield stress in compression, shows the strong mode of behaviour, whereas the medium-dense bonded material of the higher yield stress shows the weak mode (these two bonded materials both have  $R = 1$  MN). Hence, Fig. 11c confirms the third Coop and Willson criterion concerned with initial density.

Figures 10 and 11 show that DEM is a useful tool in examining the bonding effect in natural soils.

### 3.4 Penetration Mechanism in Granular Ground

The cone-penetration test is an insitu test in geotechnical engineering, in which a cone-shaped penetrometer is pushed into the ground at a constant rate. The resistance on the cone tip is measured and is then related to soil classification and soil properties. However, the penetration mechanism is still not very clear, due to the complex of the boundary-value problem which involves: (a) large relative sliding on the soil-penetrometer interface; (b) large deformation of the soil; (c) the high gradient of the field variables around the penetrometer, and (d) the soil involved undergoing an complex stress-path which is evidently different from that representative of the conventional laboratory tests. We shall introduce some plane-strain penetration mechanism in granular material using DEM, which is described in terms of displacement path and stress field. The detailed observation can be found in the reference [23]. We use DEM, because it can capture the aforementioned four features easily.

The contact mode used is a standard contact laws shown in Fig. 1. The material used is composed of 20 types of disks with a maximum diameter of 3.525 mm, a minimum diameter of 2.25 mm, an average grain diameter  $d_{50} = 2.925$  mm and uniformity coefficient  $d_{60}/d_{10} = 1.25$  [23]. Take advantage of the geometric symmetry of the problem, only half of the ground and half of the penetrometer are considered in the analyses. The target ground consists of 10,000 particles with planar void ratio of about 0.24, and has a depth and width as  $16R$  and  $17.5R$ , respectively, where  $R$  represents the half-width of the penetrometer. The multi-layer under-compaction method [19] was used to generate the ground. After the ground is generated, half of a standard penetrometer with its radius as  $R = 18$  mm and its apex angle as  $60^\circ$ , is formed over the ground, as shown in Fig. 12. The penetrometer is described with three rigid walls, i.e. a frictional wall to simulate penetrometer *tip*, vertical frictional and frictionless walls to simulate penetrometer *sleeves*. The effect of tip-soil friction is to be clarified by choosing different frictional coefficient  $\mu$  between the tip (or frictional sleeve) and particles. For simplicity, a perfectly-smooth (P-S) and a perfectly-rough (P-R), i.e.  $\mu = 0$  and  $\mu = \tan \phi_\mu$ , respectively, are considered. The penetrometer is pushed downward at  $2 \text{ mm s}^{-1}$  (around  $0.1 \text{ R s}^{-1}$ ). The  $K_0$  boundaries are used reduce possible boundary effects [23].

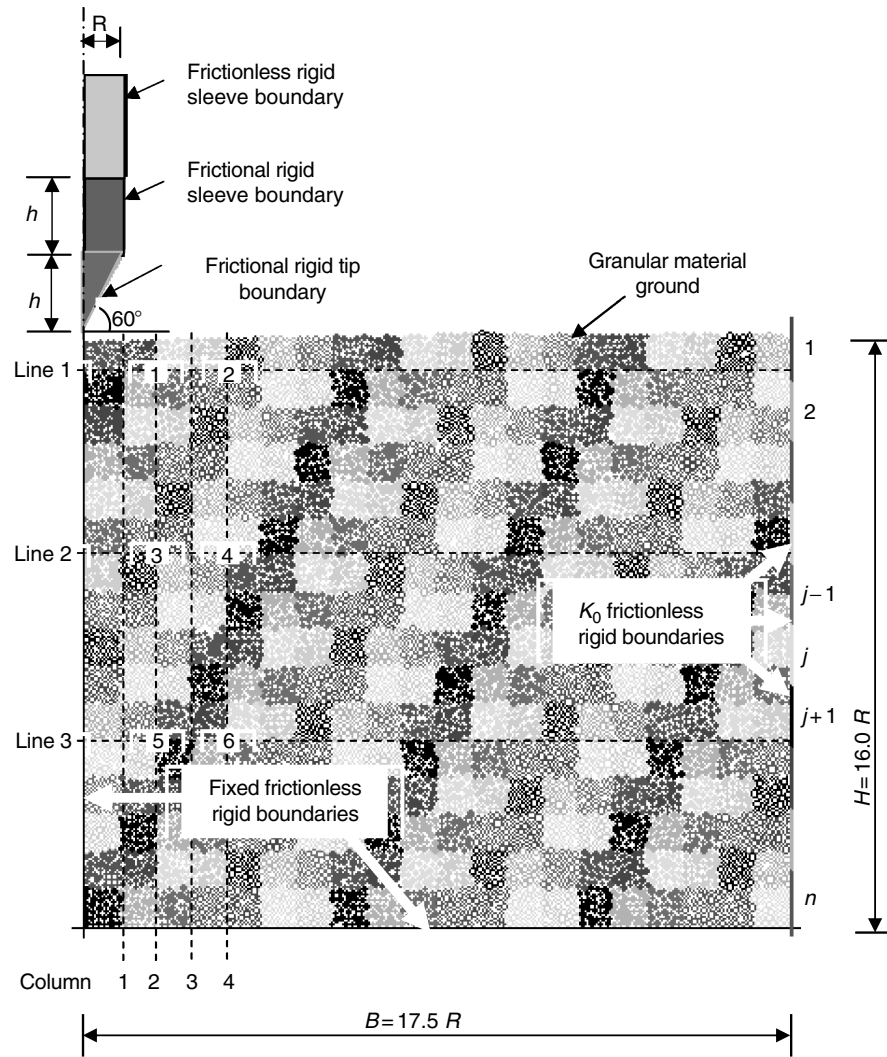


**Fig. 12.** Boundary conditions and observance positions in DEM penetration tests

Figure 13 provides the tip resistances ( $q_c$ ) and their normalized values by the initial vertical stress ( $q_c/\sigma_{v0}$ ), measured continually during the penetration in both P-R and P-S cases. Figure 13a shows that  $q_c$  increases with penetration depth with its initial gradient larger than the latter one in both cases. At the same depth, the P-R leads to  $q_c$  larger than the P-S as expected. Figure 13b shows that  $q_c/\sigma_{v0}$  initially increases, then decreases, and finally approaches a constant with depth. This is in agreement with that observed in centrifuge modelling [4].

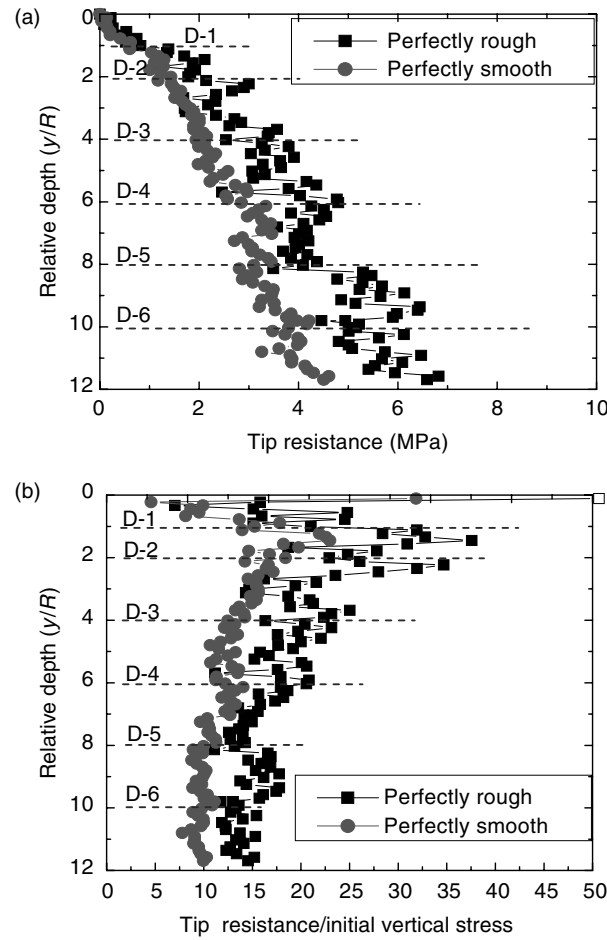


**Fig. 13.** Tip resistances, and their normalized values in DEM penetration tests

Figure 14 presents the displacement paths of the grid nodes on lines 1–3 (see Fig. 12). The vertical displacement is shown on an amplified scale in the figure. Figure 14 shows that:

- (a) The final positions of the nodes on line 1 are all above their initial positions in both the perfectly-rough (P-R) and perfectly-smooth (P-S) cases. The nodes of  $X/R > 2$  move upward and sideward, and their final position moves down with  $X/R$ . In contrast, those grid nodes of  $X/R \leq 2$  initially moves downward and then upward while moving sideward (“hook” shape), and their final position moves up with  $X/R$ . The tip-soil friction shows evident influence on the displacement path of the nodes of  $X/R \leq 2$ , with the P-R leading to a larger downward displacement than the P-S.

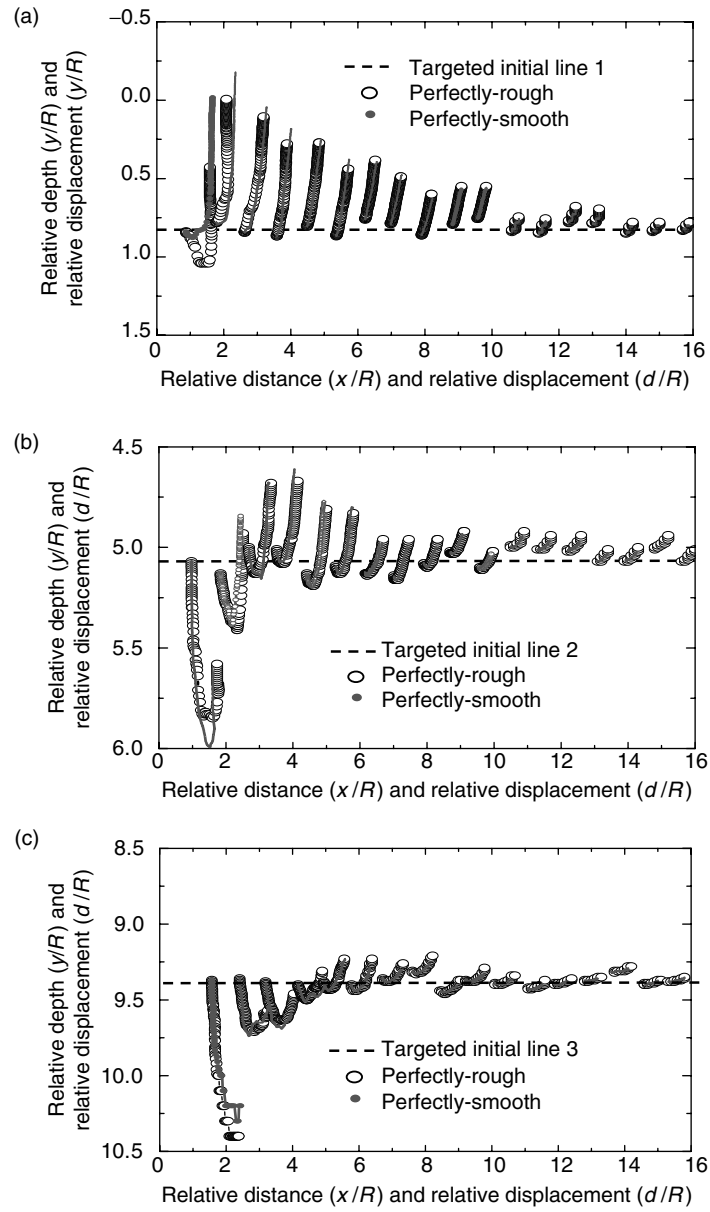


**Fig. 14.** Displacement paths of grid nodes on lines 1–3 (a–c) in DEM penetration tests

- Furthermore, the P-R leads to a smaller upward displacement within  $X/R \leq 6$  but a larger upward displacement for  $X/R \geq 6$  than the P-S.
- (b) On line 2, the final positions of the nodes are all above their initial positions in both P-R and P-S cases except for those nodes of  $X/R \leq 1$ . In addition, the final position of the nodes moves up with the increasing of  $X/R$  until  $X/R = 4$ , then moves down with  $X/R$ . The nodes of  $X/R \leq 9$  show “hook” shape displacement path, while the grid nodes of  $X/R > 9$  undergo only upward and sideward motions. The magnitude of downward motion is as large as about  $R$  for the node at  $X/R = 1$ , and decrease greatly with the increasing of  $X/R$ . Again, the tip-soil friction shows evident influence on the displacement path of the nodes of  $X/R \leq 2$ . Generally, the P-R leads to a smaller upward displacement within  $X/R \leq 6$  but a larger upward displacement  $X/R \geq 6$  than the P-S.
  - (c) The behaviour of grid nodes on line 3 is similar to that on line 2. However, all the nodes show evidently larger downward motions. The final positions of the grid nodes of  $X/R \leq 3$  are all below their initial positions in both the P-R and P-S cases, while others are above the corresponding initial positions. The “hook” shape range is up to  $X/R = 11$  and moreover the nodes of  $X/R = 1$  move only downward and sideward.

Figure 15 provides the distributions of major and minor principal stress vectors during the tests. In the figure, the maximum major stresses are plotted by a vector of a constant length in order to illustrate the distributions clearly, although the maximum major stress differs in the perfectly-rough (P-R) and perfectly-smooth (P-S) cases and changes with penetration depth. Figure 15 shows that

- (a) The penetration has great effect on the stress distribution in the area near the penetrometer, where high gradient of stresses including the values and directions is observed as expected. The maximum stresses occur near the tip, with its major principal stress nearly perpendicular to the tip;
- (b) In the area close to the penetrometer, all the major principal stresses tend to be in a direction to the penetrometer centre. In the area far from the penetrometer, the penetration effect is very small, and hence the principal stresses are predominately controlled by the self-gravity with the major principal stress in the vertical direction as expected.
- (c) The stresses beneath the tip point are larger in the P-R than in the P-S. This is consistent with the observation in Fig. 14 that the P-R leads to larger downward motion of the particles beneath the tip point than the P-S. In addition, the major principal stress near the tip has a larger inclination to  $Y$ -axis in the P-R than in the P-S, probably due to the shear force on the tip which is induced by the tip-soil friction.

Figures 13–15 show that DEM is also a useful tool to some complex boundary value problems in geotechnical engineering.

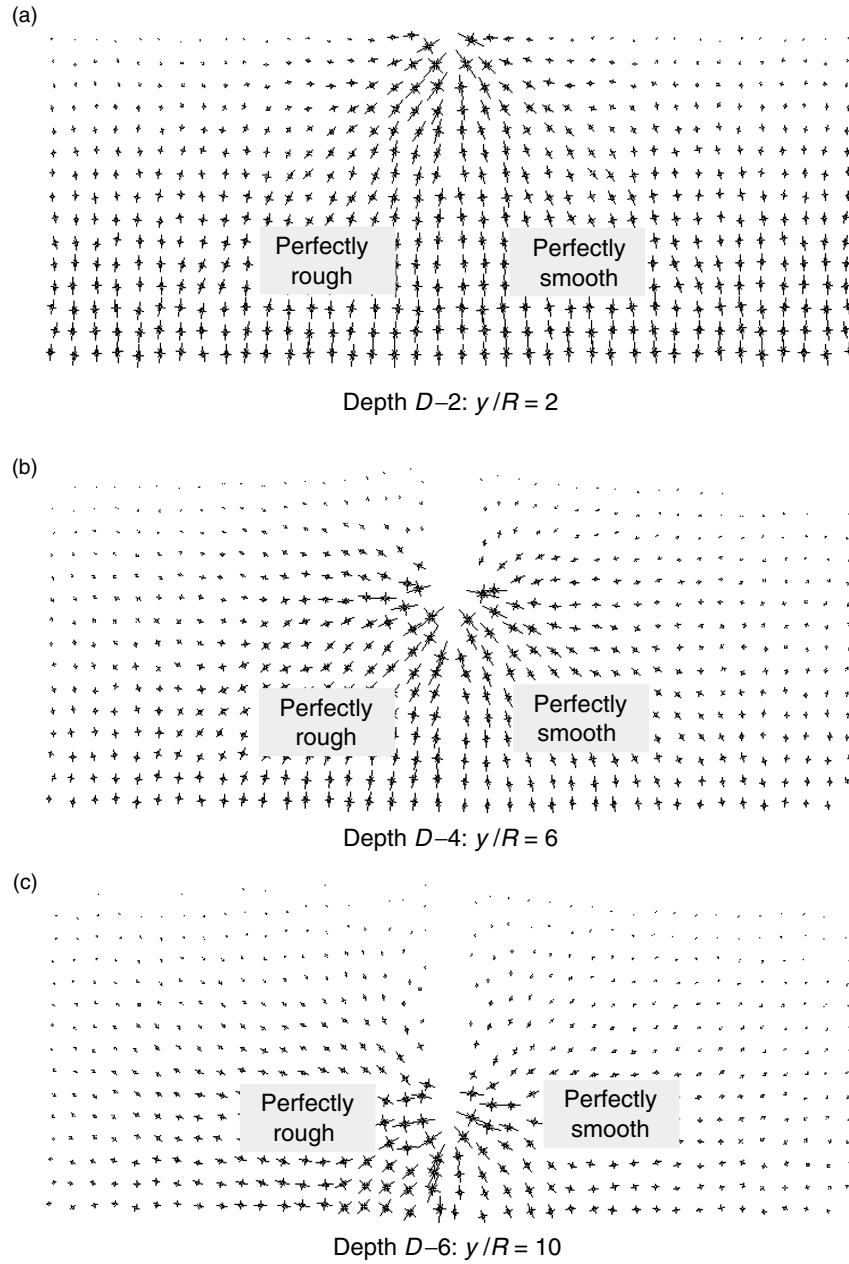


**Fig. 15.** Distributions of major and minor principal stress vectors in DEM penetration tests

## 4 Concluding Remarks

This chapter introduced recent application of the DEM to geomechanics, which is limited to the work related to the first author's two postdoctoral fellowships in Canada and UK and which are concerned with main topics in this workshop. It can be drawn from these application examples that:

- (a) DEM is a numerical simulation technique that treats soils as an assembly of discrete materials, and can efficiently provide their macroscopic–microscopic responses under loading. The behaviour of assemblies can be controlled rigorously by very simple contact laws at interparticle contacts.
- (b) One of the key issues on DEM is the contact laws at interparticle contacts. Different contact laws have been introduced and are found useful for investigating noncoaxiality of granular materials, effective stress in unsaturated soils, bonding effect in natural soils and penetration mechanism in granular ground.
- (c) DEM is a very promising tool to solve some problems not only in fundamental geomechanics but also in complex boundary value problems in geotechnical engineering, which are difficult to solve by other geomethods.

## Acknowledgements

The authors thank the EPSRC, UK with grant number GR/R85792/01; NSERC, Canada, for the financial support of the first author during his two postdoctoral fellowships. The contributions to the work in this article from Prof. Serge Leroueil and Prof. Jean-Marie Konrad, Department of Civil Engineering, Laval University, Canada; Dr. David Harris, School of Mathematics, The University of Manchester, UK are greatly appreciated.

## References

1. Bardet J.P. and Proubet J. (1991). A numerical investigation of the structure of persistent shear bands in granular media. *Géotechnique*, 41: 599–613
2. Bardet J.P. and Vardoulakis I. (2001). The asymmetry of stress in granular media. *International Journal of Solids and Structures*, 38(2): 353–367
3. Bishop A.W. (1959). The principle of effective stress. *Teknisk Ukeblad*, 106(39): 859–863
4. Bolton M.D. and Gui M.W. (1993). The study of relative density and boundary effects for cone penetration tests in centrifuge. Research report: CUED/D-SOILS/TR256, Dept. of Engrg., Cambridge University, UK
5. Chang C.S. and Liao C.L. (1990). Constitutive relation for a particulate medium with effect of particle rotation. *International Journal of Solids and Structures*, 26: 437–453

6. Chang C.S. and Ma L. (1991). A micromechanically-based micropolar theory for deformation of granular solids. *International Journal of Solids and Structures*, 28(1): 67–86
7. Cheng Y.P., Nakata Y. and Bolton M.D. (2003). Discrete element simulation of crushable soil. *Géotechnique*, 53(7): 633–641
8. Christoffersen J., Mehrabadi M.M., Nemat-Nassar S. (1981). A micromechanical description on granular material behaviour. *ASME, J. Appl. Mech.*, 48: 339–344
9. Coop M.R. and Willson S.M. (2003). On the Behavior of Hydrocarbon Reservoir Sands and Sandstones. *J. Geotech. Eng. ASCE*, 129(11): 1010–1019
10. Cundall P.A. and Strack O.D.L. (1979). The distinct numerical model for granular assemblies. *Géotechnique*, 29: 47–65
11. Ehlers W., Ramm E., Diebels S. and D’Addetta G.A. (2003). From particle ensembles to Cosserat continua: homogenization of contact forces towards stresses and couple stresses. *International Journal of Solids and Structures*, 40(24): 6681–6702
12. Fisher R.A. (1926). On the capillary forces in an ideal soil. *Journal of Agricultural Science*, 16: 492–505
13. Fredlund D.G. and Rahardjo H. (1993). *Soil mechanics for unsaturated soils*. Wiley Publications, New York
14. Iwashita K. and Oda M. (1998). Rolling resistance at contacts in simulation of shear band development by DEM. *Journal of Engineering Mechanics, ASCE*, 124(3): 285–292
15. Jennings J.E. and Burland J.B. (1962). Limitations of the use of effective stresses in partly saturated soils. *Géotechnique*, 2(2): 13–19
16. Jiang M.J. and Harris D. (2003). Generalized effective stress in unsaturated granulate by DEM analysis. *Int. Conf.: From Experimental Evidences Towards Numerical Modelling of Unsaturated Soils*, Weimar, Germany, September 18th–19th, 2003, Vol. II, pp. 201–214
17. Jiang M.J., Harris D. and Yu H.-S. (2005a). Kinematic models for non-coaxial granular materials: Part I: theories. *International Journal for Numerical and Analytical Methods in Geomechanics*, 29(7): 643–661
18. Jiang M.J., Harris D. and Yu H.-S. (2005b). Kinematic models for non-coaxial granular materials: Part II: evaluation. *International Journal for Numerical and Analytical Methods in Geomechanics*, 29(7): 663–689
19. Jiang M.J., Konrad J.M. and Leroueil S. (2003). An efficient technique to generate homogeneous specimens for DEM studies. *Computers and Geotechnics*, 30(5): 579–597
20. Jiang M.J., Leroueil S. and Konrad J.M. (2002). DEM study of microstructured soil. 55th CSCE-ASCE conference, Hamilton, Ontario, Canada, pp. 313–320
21. Jiang M.J., Leroueil S. and Konrad J.M. (2004). Insight into strength functions in unsaturated granulate by DEM analysis. *Computers and Geotechnics*, 31(6): 473–489
22. Jiang M.J. and Shen Z.J. (1996). A structural suction model for structured clays, In: 2nd International Conference on Soft Soil Engineering (eds. Z.J. Shen et al.). Nanjing, China, pp. 213–247
23. Jiang M.J., Yu H.-S. and Harris D. (2005c). Discrete Element Modelling of Deep Penetration in Granular Soils. *Numerical and Analytical Methods in Geomechanics*, 30(4): on-line

24. Jiang M.J., Yu H.-S. and Leroueil S. (2005d). A simple and efficient approach to capturing bonding effect in natural sands by DEM. (Submitted to Int. Journal for Numerical and Analytical Methods in Engineering for publication)
25. Kiyama H., Nishimura T. and Fujimura H. (1994). Advanced distinct element model coupling with pore water. *Doboku Gakkai Rombun-Hokokushu/Proceedings of the Japan Society of Civil Engineers*, 499 (III-28), pp. 31–39
26. McDowell G.R. and Harireche O. (2002). Discrete element modelling of soil particle fracture. *Géotechnique*, 52(2): 131–135
27. Ng T.T. and Dobry R. (1994). A nonlinear numerical model for soil mechanics. *Journal of Geotechnical Engineering, ASCE*, 120(2): 388–403
28. Oda M., Konishi J. and Nemat-Nasser S. (1982). Experimental micromechanical evaluation of strength of granular materials: effects of particle rolling. *Mechanics of Materials*, 1: 269–283
29. Shen Z.J. (1999). A granular medium model for liquefaction analysis of sands. *Chinese Journal of Geotechnical Engineering*, 21(5): 742–748
30. Thornton C. (2000). Numerical simulation of deviatoric shear deformation of granular media. *Géotechnique*, 50(1): 43–53
31. Thornton C. and Barnes D.J. (1986). Computer simulated deformation of compact granular assemblies. *Acta Mechanica*, 64: 45–61
32. Wan R.G. and Guo P.J. (2004). Stress dilatancy and fabric dependencies on sand behaviour. *Journal of Engineering Mechanics, ASCE*, 6(1): 635–645
33. Anandaraman A. (2000). On influence of fabric anisotropy on the stress-strain behaviour of clays. *Computers and Geotechnics*, 27: 1–17.
34. Iwashita K. and Oda M. (2000). Micro-deformation mechanism of shearbanding process based on modified distinct element. *PowderTechnol*, 109: 192–205.
35. Kuhn M.R. and Mitchell J.K. (1993). New perspectives on soil creep. *Journal of Geotechnical Engineering, ASCE*, 119(3): 507–524.
36. Harris D. (1995). A unified formulation for plasticity models of granular and other materials. *Proc. R. Soc. Lond.*, A450: 37–49.





<http://www.springer.com/978-3-540-25135-4>

Modern Trends in Geomechanics

Wu, W.; Yu, H.-S. (Eds.)

2006, X, 560 p., Hardcover

ISBN: 978-3-540-25135-4